Materials Science in Semiconductor Processing 176 (2024) 108308

Contents lists available at ScienceDirect

Materials Science in Semiconductor Processing

journal homepage: www.elsevier.com/locate/mssp

Selective Epitaxy of Germanium on silicon for the fabrication of CMOS compatible short-wavelength infrared photodetectors

Diana Ryzhak [a,*], Agnieszka Anna Corley-Wiciak [a], Patrick Steglich [a], Yuji Yamamoto [a], Jacopo Frigerio [b], Raffaele Giani [b], Andrea De Iacovo [c], Davide Spirito [a], Giovanni Capellini [a,d]

[a] IHP – Leibniz-Institut für Innovative Mikroelektronik, Im Technologiepark 25, 15236, Frankfurt (Oder), Germany
[b] L-NESS, Dipartimento di Fisica del Politecnico di Milano, Via Anzani 42, 22100, Como, Italy
[c] Dipartimento di Ingegneria Industriale, Elettronica e Meccanica - Università Roma Tre, Via Vito Volterra 62, 00146, Roma, Italy
[d] Dipartimento di Scienze, Università Roma Tre, V.le G. Marconi 446, 00146, Roma, Italy

ARTICLE INFO

Keywords:
Germanium
Reduced-pressure chemical vapor deposition (RP-CVD)
Selective epitaxial growth (SEG)
Strain
Micro-photoluminescence (μ-PL)
Photodiode

ABSTRACT

Here we present the selective epitaxial growth of Ge on Si using reduced pressure chemical vapor deposition on SiO_2/Si solid masks realized on 200 mm Si wafers, aiming at manufacturing integrated visible/short-wavelength infrared photodetectors. By a suitable choice of the reactants and of the process conditions, we demonstrated highly selective and pattern-independent growth of Ge microstructure featuring high crystalline quality. The Ge "patches" show a distinct faceting, with a flat top (001) facet and low energy facets such as e.g. {113} and {103} at their sidewalls, independently on their size. Interdiffusion of Si in to the Ge microcrystals is limited to an extension of ~20 nm from the heterointerface. The Ge patches resulted to be plastically relaxed with threading dislocation density values better or on par than those observed in continuous two-dimensional Ge/Si epilayer in the low 10^7 cm^{-2} range. A residual tensile strain was observed for patches with size >10 μm, due to elastic thermal strain accumulation, as confirmed by μ-Raman spectroscopy and μ-photoluminescence characterization. Polarization-dependent Raman mapping highlights the strain distribution associated to the tridimensional shape. On this material, Ge photodiodes were fabricated and characterized, showing promising optoelectronic performances.

1. Introduction

Germanium (Ge) is considered a key player in the microelectronic industry thanks to the variety of applications in electronic and optoelectronic devices manufactured using the silicon-based CMOS technology [1]. In particular, Ge is the active material in high performance short-wavelength infrared (SWIR) waveguide photodetectors (PDs) [2] to be integrated in the silicon photonics platform for wide band data transmission [3]. Recently, it has been proposed the use of Ge for the fabrication of VIS/SWIR vertical PD [4,5], since this spectral range is of high interest for a score of different applications ranging from automotive, to environmental monitoring to security screening [6]. Indeed, Ge-based VIS-SWIR camera could be very attractive since the current "off the shelf technologies" are mainly based either on photodetectors made of compound semiconductors (such as InGaAs/InP, GaAsSb/GaAs, or HgTe) or, more recently, on PbS quantum dots-based imagers [7]. All these materials require a rather complex process flow for fabrication of PDs, and are difficult to integrate with standard CMOS read-out electronics, leading to a high cost per device (reaching the k€ range). Furthermore, they are difficult to operate under low light or harsh environmental conditions.

Typically, VIS-SWIR imaging cameras reach VGA-standard resolution, i.e. they are made of arrays of 640 × 480 up to a maximum of 1280 × 1024 individual photodetector. To monolithically integrate such a large number of Ge vertical photodetectors together with Si microelectronics, the most reasonable approach is, as was already developed for waveguide PDs, to use front-end of the line process to deposit Ge on selected area of the silicon substrates, defined by lithography via the so-called selective epitaxial growth (SEG) [8]. However, the fabrication of vertical Ge PDs on silicon (Si) has much more stringent process constrains as compared to the waveguide PDs, since a larger Ge thickness is required to increase the PD responsivity. In fact, this requirement might conflict with other steps of the back end of line.

As such, the major challenge is to develop a Ge SEG on Si substrates

* Corresponding author.
E-mail address: ryzhak@ihp-microelectronics.com (D. Ryzhak).

https://doi.org/10.1016/j.mssp.2024.108308
Received 6 December 2023; Received in revised form 1 March 2024; Accepted 2 March 2024
Available online 11 March 2024

process that allows a very high control of the Ge thickness and thickness uniformity, a low density of defects (threading dislocations) originated by the plastic relaxation of the Ge/Si heterostructure, a high selectivity to avoid Ge growth in unwanted regions of the wafer, a controlled shape of the deposited material to allow for further processes (such as contact formation), and, possibly, a pattern-independent growth to allow for more robust fabrication.

Here we investigate the outcome of reduced pressure chemical vapor deposition (RP-CVD) based SEG process carried out in a 130 nm SiGe BiCMOS pilot line operating with 200 mm silicon substrates [9]. This study aims to provide insight into sample geometry and orientation employing a detailed analysis of polarization-dependent Raman spectroscopy and mapping to understand these complex relationships. In particular, we thoroughly investigated the morphology, the selectivity and the optical properties of Ge SEG patches of different size and arrangement and we show preliminary results on the optoelectronic characterization of Ge/Si PDs made of this material that demonstrate the viability of such technological platform for the realization of integrated VIS/SWIR imagers.

2. Experimental

SEG of Ge on SiO_2/Si patterned substrate was carried out using RP-CVD system. The samples were fabricated on 200 mm p-type Si (001) substrate. 70 nm thick SiO_2 was deposited by CVD using Tetraethylorthosilicate onto the Si substrate. Then 2–10 μm square windows with <110> oriented sidewalls with 7–40 μm pitch were structured by photolithography and dry etching. In order to prevent surface damage, the top 20 nm of SiO_2 were removed by wet etching. Afterward, the wafer was cleaned by standard Radio Corporation of America clean followed by 0.5% HF dip to remove native oxide in the windows. At this point, SiO_2 mask thickness was 50 nm. After the HF last clean, the wafer was loaded in into the RP-CVD reactor, and prebaked at 850 °C in H_2 gas to remove residual oxide on Si surface. Thereafter, the wafer was cooled down to 350 °C. During the cooling, carrier gas was switched from H_2 to N_2 to form hydrogen-free Si surface. Then Ge seed layer was selectively deposited using an N_2-GeH_4 gas mixture. After the Ge seed layer growth, the main part of deposition was performed at 550 °C using H_2-GeH_4 gas mixture. To improve crystal quality, several cycles of annealing steps at 800 °C were introduced by interrupting the Ge growth [10]. The thickness of the RP-CVD of Ge patches was selected to be compatible with further processing in the back end of the line (BEOL) between 500 and 700 nm. Four anneal cycles were carried out for a thickness of 500 nm and five for 700 nm.

Secco defect etching was used for etch pit count, to measure the threading dislocation density (TDD). Scanning electron microscope (SEM) is used to analyze and quantify the surface pits. In order to measure Si diffusion in Ge near the interface, Time-of-Flight Secondary Ion Mass Spectrometry (ToF-SIMS) was used. ToF-SIMS was completed with a positive polarity, sputtering was achieved with O2 ions at 500 eV over a 300×300 μm^2 area. The morphology of Ge patches was evaluated through atomic force microscopy (AFM) in tapping mode (Bruker Dimension Icon, Nanoscope V software). Raman spectra were obtained with a Renishaw in Via Microscope system with a 532 nm wavelength laser and a power of 0.13 mW, equipped with a 3000 lines/mm grating. An objective with a numerical aperture (NA) 0.9 and a spot size of ~400 nm was used. μ-PL measurements were obtained with a HORIBA iHR 320 spectrometer with a 600 lines/mm grating, equipped with a Synapse/Symphony InGaAs II detector, an objective of 50×, and an infrared laser of 1064 nm wavelength with a power of 17.4 mW. The temperature dependence was determined by using a liquid-nitrogen flow cryostat. All spectra were collected in backscattering geometry, and the setup response was calibrated using a white lamp.

For fabrication of PDs, a sample with Ge thickness of 700 nm was selected, and a ~50 nm thick non-selective P-doped Si layer with ~1×10^{19}cm^{-3} was deposited as capping layer to realize a top contact. Then the wafer was post-processed as follows. Square photodiodes with lateral dimensions comprised between 45 and 480 μm were then fabricated on selected large patches of the sample. The top and bottom contact windows were defined by laser lithography with a Heidelberg MLA 100 mask less aligner. Ohmic contacts on both the top polysilicon layer (n-contact) and on the Si substrate (p-contact) were then realized by depositing a Ti (10 nm)/Au (100 nm) metal stack with an Unaxis BAK 640 e-beam evaporation tool, followed by a lift-off process.

For photodiodes characterization, a Keithley 2450 source meter unit was employed to measure DC current-voltage curves in the dark. Photoresponse was obtained using a calibrated broadband light source (1100–1650 nm) and a monochromator, and the light was shined on the device through an optical fiber. The intensity of the light was modulated by a mechanical chopper at 330 Hz. The photocurrent generated by the photodiode was collected by microprobes and then fed to a transimpedance stage to convert it into a voltage signal, which was measured by a lock-in amplifier.

3. Results and discussion

3.1. Morphology, composition and TDD of Ge patches

We fabricated different structures for the purposes of characterization of the material, for the analysis of the optical properties and finally for the PDs. Square patches of width 2–10 μm in arrays with pitch of 7–40 μm (as shown in Fig. 1 (a,b) and Table 1) allowed to study the details of the SEG process in terms of morphology and strain relaxation, and the related optical properties. This size range was chosen in view of a possible application of this material to the manufacture of relatively dense pixel arrays. Larger control structures, having lateral size between 50 and 600 μm^2 were used for structural and chemical characterization (e.g. via ToF-SIMS and cross-sectional SEM). Furthermore, on these structures vertical PDs of lateral size 45–480 μm were fabricated.

In Fig. 1 we show a SEM image of a SEG Ge in a SiO_2/Si hard-mask, with a square arrangement of 100 5×5 μm^2 wide and 500 nm-thick Ge three dimensional microcrystals ("patches") separated by a pitch of 10 μm. The SEG process was found to be highly selective, without any Ge seeds on the SiO_2 mask throughout the whole wafer.

All the Ge patches, investigated by AFM as shown in Fig. 2 (a), had a truncated pyramid shape with a top plateau and faceted edges, independently of their width and thickness. The cross-section of 500-nm-thick patches of width 2, 3, and 5 μm in Fig. 2 (b) showed that different growth window sizes did not affect the slopes of the edges, but the plateaus widened for larger patch size due to the energetic favorability of the (001) facet over the exposed surface. As long as growth parameters remain relatively constant, increasing the thickness of the Ge patches from 500 nm to 700 nm did not lead to significant changes in the slope or plateau appearance. The consistent height and slope observed over different patches with variations in width, specifically comparing 500 nm to700 nm thick patches, offer valuable shape predictability to calculate the area of the top flat region.

To gain insight in the morphology of the patches, we analyzed the facets according to the method described in refs. [11,12], finding well pronounced facets {113}, {117} [13], {103}, and {223} [14], whose extension was almost patch width-independent. Fig. 3 (a,b,c) show the Ge faceting distribution with a 3D view and a stereographic map of a 10×10 μm^2 patch. With respect to the (001) plane, the non-centered spots had polar angles of 25.3° and 46.5°, which correspond to {113} and {223} facets, respectively [15]. Spots in another group are at 11.3° and 18.8°, corresponding to facets {117} and {103} [13]. Remarkably, these facet orientations are all compatible with previous findings on nanometric size, elastically relaxed Ge/Si islands which grow following the Stranski-Krastanov dynamics. This points to the dominant effect of the surface energy density in determining the patch shape versus the lattice strain [16]. Moreover, epitaxial growth of semiconductor materials, such as Ge/Si patches, commonly exhibits the (001) facet,

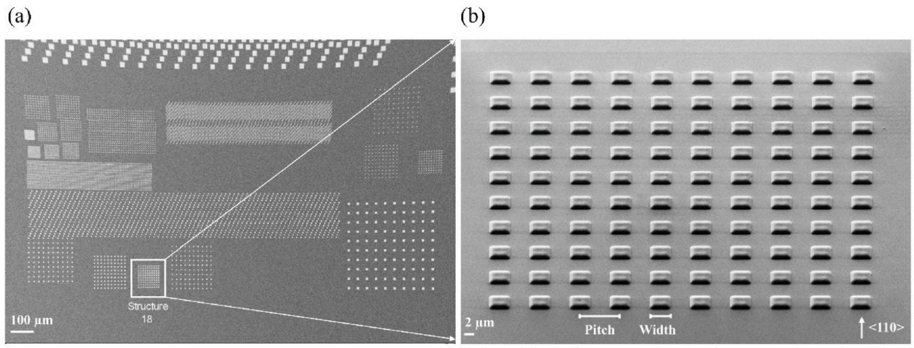

Fig. 1. (a) SEM plan view of a SEG Ge sample, with various patches arrays. (b) Magnification of Ge patch of 5 × 5 µm^2. Definition of Pitch and Width are marked.

Table 1
Width and pitch of the patches under investigation.

Width [µm]	Pitch [µm]
2	7
3	4
5	10,15,20
10	40

corresponding to a high-symmetry plane perpendicular to the growth direction [16]. Due to its low surface energy, the (001) facet tends to have a flat and smooth morphology if relaxed [11]. Also, {103} and {117} facets introduce a tensile strain on the surface, which can counterbalance the compressive strain from the lattice mismatch. The truncation phenomenon of Ge structures is closely related to strain plastic relaxation and has been described in the literature [17].

From AFM topography, the volume of each patch was calculated, and reported in Fig. 4 (a) for width 5 µm at different pitch size (10, 15 and 20 µm). The volume, and thus the growth rate, was nearly independent of the pitch size. We also used ToF-SIMS to investigate SiGe interdiffusion at the heterointerface, on a control patch with very large width (600 µm). Concentration profiles, shown in Fig. 4 (b), were analyzed by Fick's diffusion fits [18], and the calculated interface width was of 17 nm. Interdiffusion in such a narrow region reduces the likelihood of forming defects, with benefits toward device application.

Finally, in Fig. 5, the results of the TDD count on the patches are presented for the samples of different Ge thickness as a function of the patch width. Exemplary SEM pictures employed for the quantification of TDD is shown in Supplementary Material Fig. S1. TDD of the 500 nm sample was independent of patch width and comparable to the case of

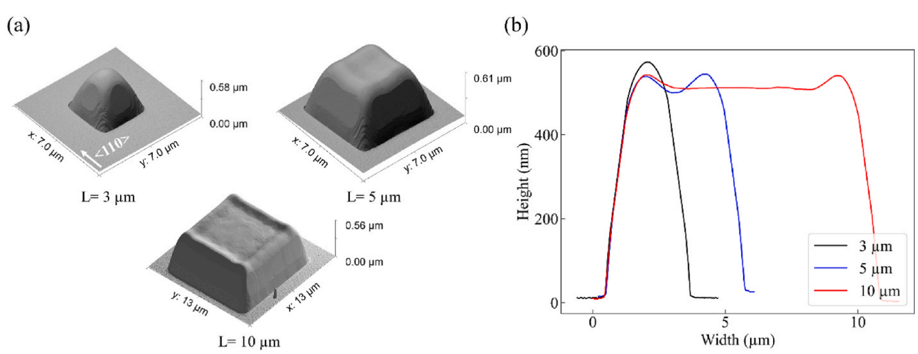

Fig. 2. (a) AFM 3D topography of 3, 5, 10 µm-wide patches. (b) Corresponding height profiles.

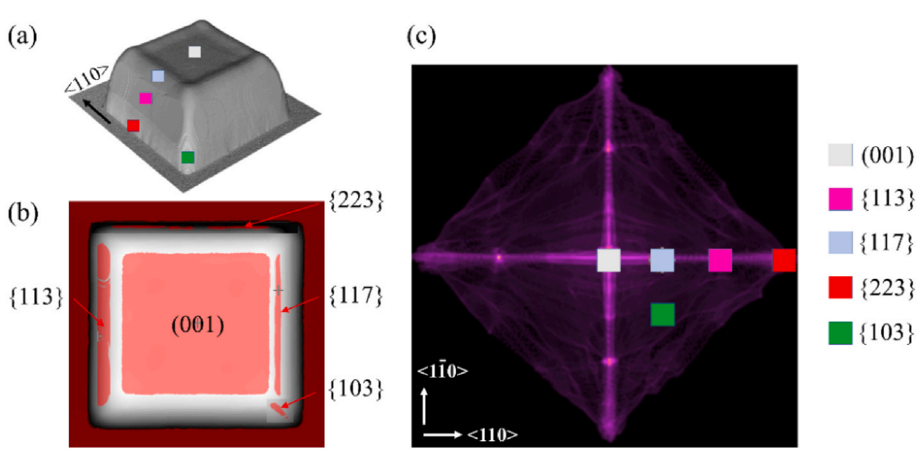

Fig. 3. (a) Identification of facets on AFM 3D topography of a 10 × 10 µm^2 patch on the 500 nm sample for different pitch sizes. (b) Faceting distribution for 10 × 10 µm^2 patch. (c) Angular distribution of the facet from AFM analysis.

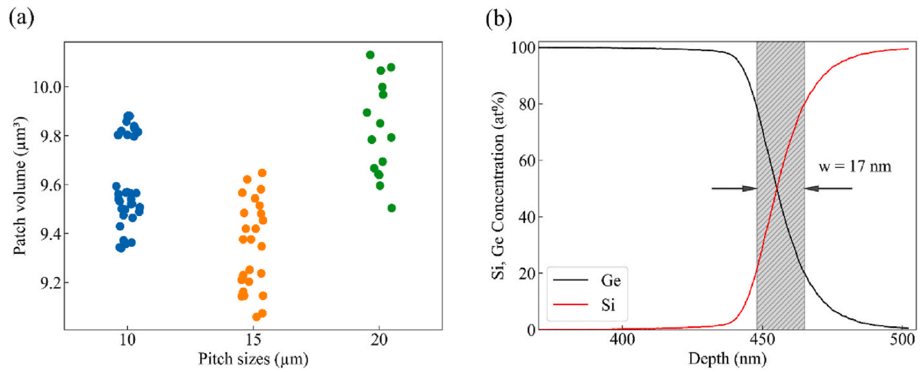

Fig. 4. (a) Volume (height × area) of 5 × 5 μm^2 patches on the 500 nm sample for different pitch sizes. (b) Si and Ge concentration at the Ge/Si heterointerface as measured by ToF-SIMS.

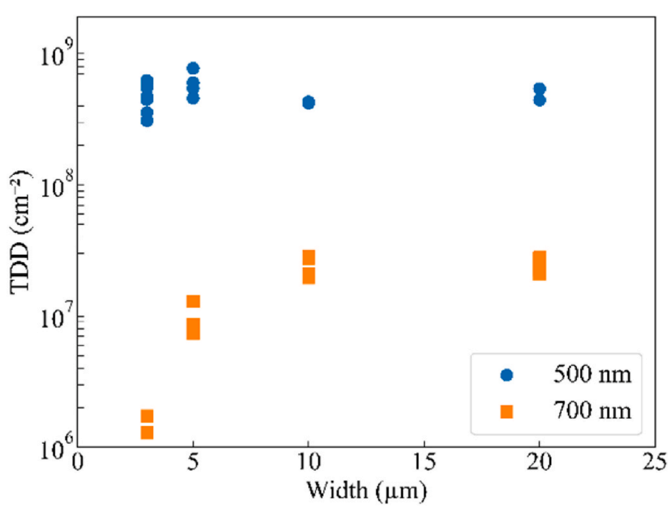

Fig. 5. TDD in patches of different width with thickness (blue) 500 nm and (orange) 700 nm.

non-SEG Ge/Si layers of the same thickness and deposited using the same process parameters [19]. The TDD was lower for thickness of 700 nm than for 500 nm at all patch widths, and for Ge/Si layer from the literature [19,20]. The primary driving force for the motion of Threading Dislocations (TDs) is their interaction with other TDs. As the thickness of a Ge patches increases, and interaction between TDs enhanced their annihilation as well. When the patch size increases from 3 μm to 10 μm, TDD increased by one order of magnitude but did not increase further at 20 μm, because the chance of an annihilation process decreases with increasing TDD, thus causing saturation. The marked drop of the TDD observed in 700 nm-thick epilayers also can be attributed to the increased capacity for dislocations to annihilate at the patches sidewalls [21,22]. This mechanism seems to be less effective in the 500 nm-thick counterparts, probably because the much higher initial TDD values observed in these samples is associated with an "hardening" of the epilayer itself, that hinders further TDD dynamics and, eventually, their annihilation at the patch sidewalls. The low TDD found in these samples indicates that SEG does not alter plastic relaxation and does not significantly impacts material quality.

3.2. Raman spectroscopy and strain

The multifaceted strained patches form an ideal system to study the effect of strain. Using polarized Raman mapping, we can at the same time evaluate the modulation of the strain on the surface of the patches with sub-μm resolution, due to the tridimensional shape, and verify the validity of common approximation in the analysis of strained layers by Raman spectroscopy. We used the backscattering configuration, and analyzed the data with the strain-shift coefficient b = −395 cm^{-1} reported in ref. [23] and a bulk Ge wafer as reference. At the center of the patch, where biaxial strain can be assumed, we observed tensile in-plane strain which increased with patch size (Fig. 6), reaching the value of a continuous Ge/Si reference layer of the same thickness as measured on a SIMS control structure. The observed higher strain in the 700 nm-10 μm structures compared to the SIMS control structure could be attributed to the variation of the strain in the patches, that can be associated to both strain distribution of the 3D shape and the surface morphology.

To have more insight in the strain distribution, we employed polarization-resolved μRaman measurement in two configurations, as shown in Fig. 7 (a)(b). In- and outgoing light propagated in z and $\bar{z}$ directions [24], respectively, parallel to the growth direction. Samples were aligned to the edge of the patch, i.e. in the <110> crystal directions. In parallel configuration, noted as (z(x'x') $\bar{z}$) in Porto notation, both the incident and detected polarization directions are parallel and aligned to the x' direction (corresponding to the [110] axis). In perpendicular configuration, the incident polarization is orthogonal to the detected polarization (z(x'y') $\bar{z}$), where y' =]. The longitudinal-optical (LO) mode is allowed in the parallel configuration and forbidden in the perpendicular configuration, while the transverse optical (TO) phonons are always forbidden. However, the patches

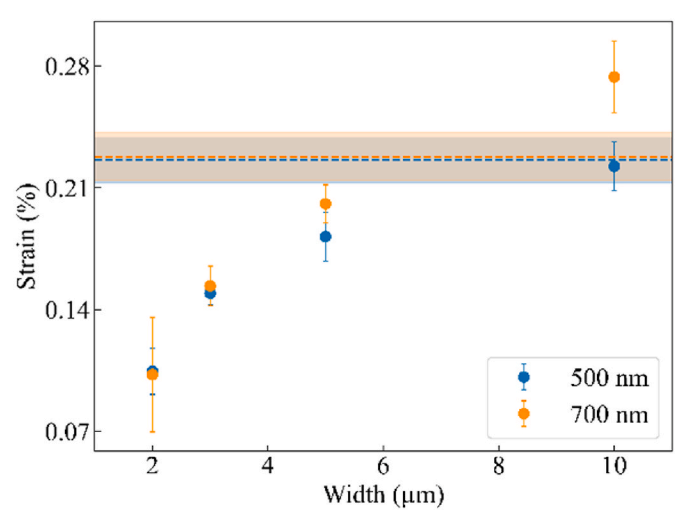

Fig. 6. Strain measured by Raman spectroscopy at the center of the patches, as a function of patch width for thickness (blue) 500 nm and (orange) 700 nm. Values are obtained from 9 points around the center of the patch, and reported as average and standard deviation. Dashed lines mark the strain value measured in the large SIMS control structures.

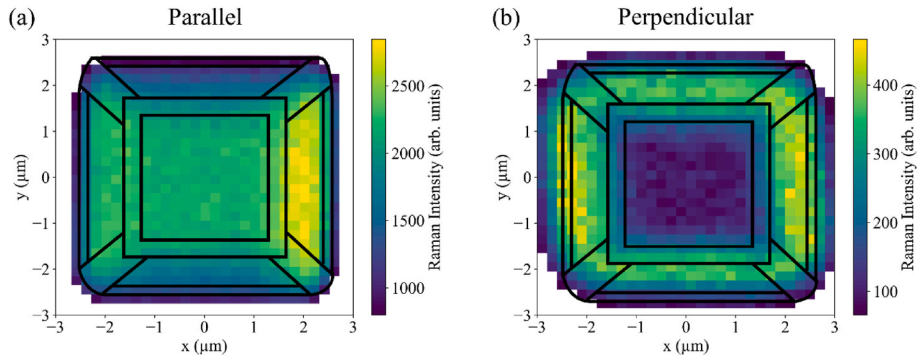

Fig. 7. Polarized Raman mapping with facet distribution of a 5 × 5 μm^2 patch with thickness 700 nm. Intensity of (a) parallel and (b) perpendicular configuration; the left right asymmetry of the measured intensities can be the effect of substrate tilt during measurements. Black lines outline the facets of the patch as measured by AFM.

provide additional strain to the system and the presence of faceting and the use of a large NA of the objective can enable the observation of TO phonons [25].

As a consequence of this selection rules, the intensity of Raman spectra (Fig. 7) for parallel configurations in center was almost ten times higher than for perpendicular configurations [26]. Also, it should be noted that in perpendicular polarization (Fig. 7 (b)) intensity was higher on the border of the patch, while the opposite occurs in parallel configuration (Fig. 7 (a)) due to crystallographic orientation of the side facets and thus to the Raman selection rules.

Also the energy of the Raman peak showed spatial dependence, with different values for parallel and perpendicular configuration (Fig. 8(a and b). In particular, we observed a spatial distribution both on the plateau and on the lateral facets (marked in Fig. 8(e)). To highlight these mode shifts, we consider the maps reported in Fig. 8 (c,d). The asymmetry observed in the Raman peak position maps (Fig. 8) may be attributed to a slight tilt in the substrate during measurements and faceting on the sample surface, so that the beam is not perfectly aligned with the (001) direction and the signal comes from an average of adjacent regions.

These were calculated as the difference between the peak positions in parallel and perpendicular configuration and the value ω_m obtained as the average of the central region of the parallel configuration in Fig. 8 (a), with $\omega_m = 299.9$ cm^{-1}, corresponding to the LO mode [27]. In this way, the maps in Fig. 8 (c,d) show the shift of the mode with respect to the LO mode. In parallel configuration (Fig. 8 (c)), on the plateau, the mode shifted to lower energy at the sides, near the {117} and {103} facets, and to higher energy at the corner near the {113} and {223} facets. In perpendicular configuration (Fig. 8 (d)), a higher energy was measured at the center of the plateau, with an average of 300.3 cm^{-1}. In the perpendicular configuration in the strained Ge, both TO and LO modes have non-null intensity, and then the measured peak is shifted with respect to the LO mode [28]. This suggests a split LO-TO modes, due to strain [29], that appeared as a single peak not resolved by the spectrometer. Indeed, the LO peak in the parallel configuration had a lower full width at half maximum (FWHM) than the LO + TO peak in the perpendicular configuration. The average FWHM in parallel was around 2.5 cm^{-1} and perpendicular 3.8 cm^{-1}. Because of the faceting, the

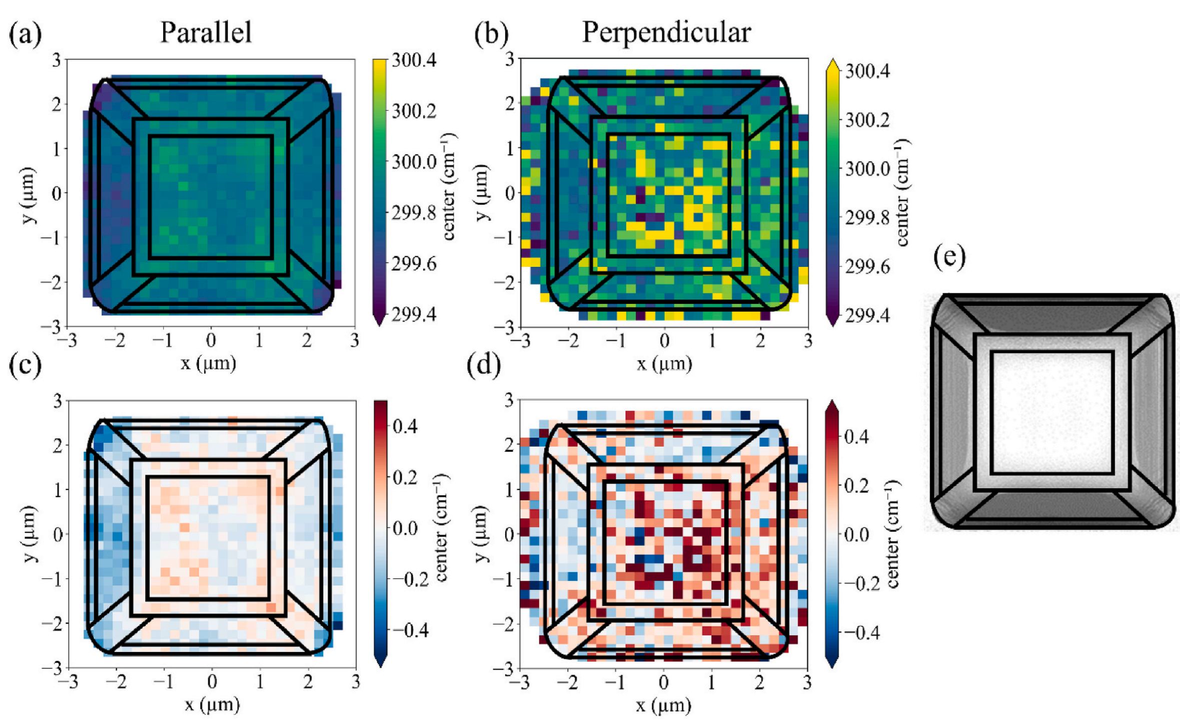

Fig. 8. (a) (b) Peak position from polarized Raman mapping of Ge 5 × 5 μm^2 for parallel and perpendicular configuration. (c) (d) Map of the difference between the peak positions and the peak position in the center of the patch in parallel configuration. (e) AFM topography with marked facets.

FWHM distribution across the patch had a spatial dependence (not shown), similar to that of the peak position in Fig. 8 (a,b).

The nature of mixed LO + TO in the perpendicular configuration is further supported by studying its dependence on patch size. Raman spectra at the center of the 5 × 5 μm^2 700 nm patch for parallel and perpendicular configuration are shown in Supplementary Material Fig. S2. The difference between the peak energy at the center of the patch in parallel and perpendicular configurations are shown in Fig. 9 for different patches and thickness, as a function of the strain calculated at the center of patch. This difference became wider as the strain increases, and can be compared with the expected splitting for LO and TO phonons given by [30].

$$\frac{\omega_s - \omega_d}{\omega_0} = \frac{-1+\alpha}{2}(p-q)\Delta\varepsilon, \tag{1}$$

where p and q are phonon deformation potentials ($p = 0.18\ \omega_0^2$, $q = -1\ \omega_0^2$), and α = 0.698 [23,31] and reported as continuous line in Fig. 9. The calculated splitting was larger in amplitude as the measured one, because in perpendicular configuration a convolution LO + TO is measured. Nonetheless, this shift is an indication of an unsuppressed TO phonon, that can be due to a non-perfectly biaxial strain in the patch, even at the center.

The dependence of strain (and thus of LO-TO splitting) on the patch size can be explained as follows. For small patches, the growth process is limited in the lateral size by the presence of the hard mask, resulting in the formation of relaxed faceted crystals. As the patch size increases, the build-up of a strained layer becomes energetically favorable over the exposed surface, approaching the case of an unpatterned layer [32]. Indeed, relaxation at the edges is expected in narrow microstructures, increasing with decreasing width [33,34], and furthermore the reduced stress in the microstructure will reduce the formation of TDs, supporting our observation in Fig. 5. As shown in the maps (Fig. 8 (c,d)), the strain is not uniform (possibly not biaxial) in the patch, and the corners of the top facet appear more relaxed than the center. This is the result of the relaxation at the edges, but also of the combined effect of the geometric constraint of the mask and the formation of the facets. Despite the complexity of the strain distribution, the possibility of demonstrated control on the strain in the patch allows to tune the optical property, as shown in the following, with great advantage in PD design.

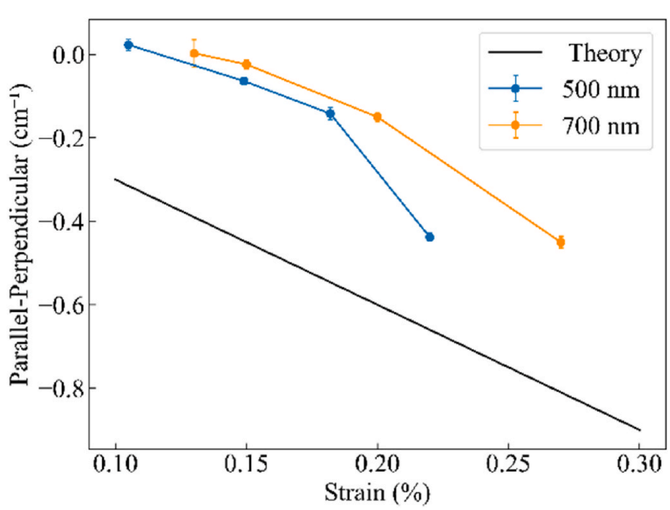

Fig. 9. Difference of the average peak position in the center of the maps in parallel and perpendicular configurations for different samples and patch size versus biaxial strain measured in the center. The black line is calculated as described in the text.

3.3. Photoluminescence and band gap

μ-PL temperature-resolved measurements were used to investigate the optical properties of the patches. In Fig. 10 (a), PL spectra are reported for patches of different width and thickness 700 nm at 80 K. High emission efficiency was observed around 0.8 eV, associated to the direct transition at the Γ point. The emission shifted to lower energy as the width of the Ge patches increased. We could also distinguish a shoulder in the spectra, assigned to radiative transition with light holes states (LH), while the main peak is associated to the heavy holes (HH) valence band. The combination of LH and HH transitions enables a wider range of energy transition, leading to strong carrier generation, that could enhance the sensitivity and responsivity of the Ge photodetector.

These spectra (Fig. 10 (b)) were investigated with the van Roosbroeck equation [31,35]. The result was studied as a function of patch width in Fig. 10 (c). A clear shift of both LH and HH transitions to lower energy was found as the width of the Ge patches increases [36], as a consequence of the increase of tensile strain. The split between LH and HH also increased (Fig. 10 (d)) as the strain of Ge increased, and the LH peak was stronger at larger strain. The significant errors are due to the fitting process sensitivity for these closely spaced energy states. The splitting followed the expected trend for Ge on Si, reported as solid line in Fig. 10 (d) [37].

Temperature dependence was measured for 2,3,5,10 μm width for all samples. The bandgap energy shifted to lower values as the temperature increases, as shown in PL spectra Fig. 11 for a 10-μm patch with thickness 700 nm. As the temperature increases, the non-radiative recombination reduces the intensity of the emission, and make the peak broader, and the splitting between the LH and HH not well-resolved (Fig. 11). The growth in intensities above 200K results from the thermal excitation of electrons to the Γ−valley of the conduction band, increasing the direct radiative recombination [38]. The emission was observed up to room temperature for larger patches, the strongest being the 10-μm patches.

3.4. Photodiode characterization

In the previous sections, we have demonstrated the control over SEG method and high crystalline quality of the Ge patches, that had low defect density enabling direct bandgap emission. For large patch width, the large tensile strain allows to extend to the optical response beyond 1550 nm. Beyond a certain width, the strain did not increase further and is dominated by the epitaxial growth of Ge/Si. These features were exploited to fabricate PDs of with lateral size of width 45–480 μm and 700 nm thickness. The use of this relatively large features lateral size makes the prototype fabrication simpler.

The dark current density of the processed photodiodes was characterized by acquiring J-V curves between -2V and 1V. In Fig. 12 (a) we show the dark current density as a function of the voltage for photodiodes of different width. Each curve was obtained by averaging J-V acquisitions of five PDs.

All the investigated photodiodes showed the expected rectifying behavior. The dark current of a reversed-biased Ge-on-Si p$^+$-i-n$^+$ photodiode is dominated by the Shockley-Read-Hall generation within the depletion region (bulk component), which is strongly enhanced by the presence of dislocations, and by the generation at the Ge surface (surface component). Such components can be evaluated by performing a linear fit of the dark current density at a specific voltage, for photodiodes featuring different size L [39,40] as expressed in the following formula:

$$J_{dark} = \frac{4L}{L^2} J_{surf} + J_{bulk} \tag{2}$$

In Fig. 12 (b) we report the dark current density values at a bias voltage of -1V, for devices with L = 480, 95, 70 and 45 μm. The values were averaged over 5 devices, and the error bars represent the standard

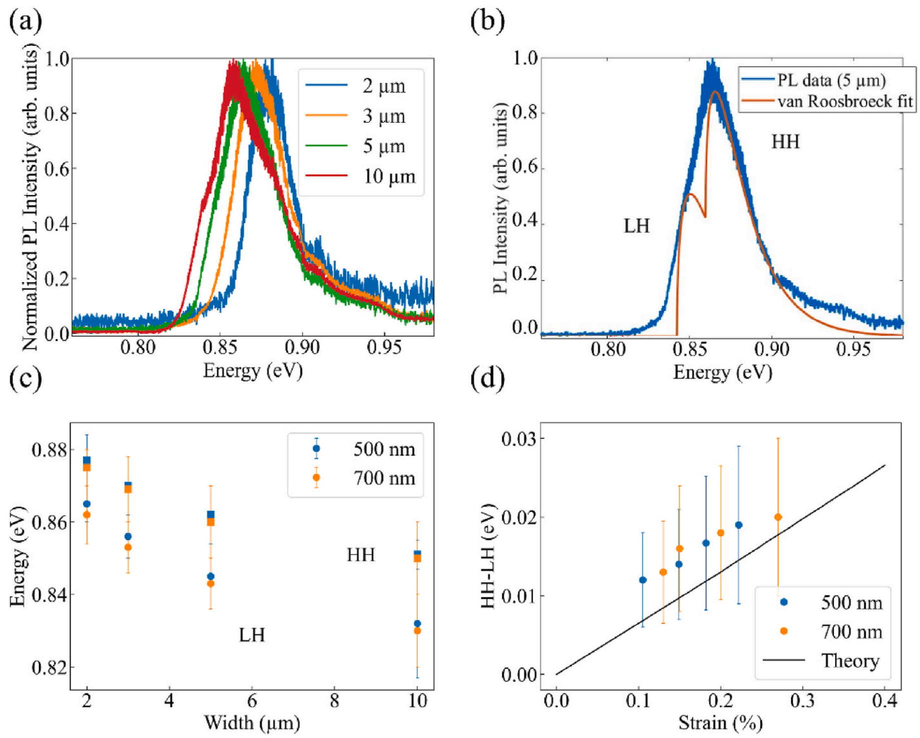

Fig. 10. (a) PL emission at 80K of a 700 nm sample normalized to unit height. (b) PL van Roosbroeck fitting of a spectrum from a patch of width 5 µm and thickness 700 nm. (c) Transition energy as a function of patch width. (d) HH-LH separation as a function of strain. The black line is a theoretical value calculated as described in the text.

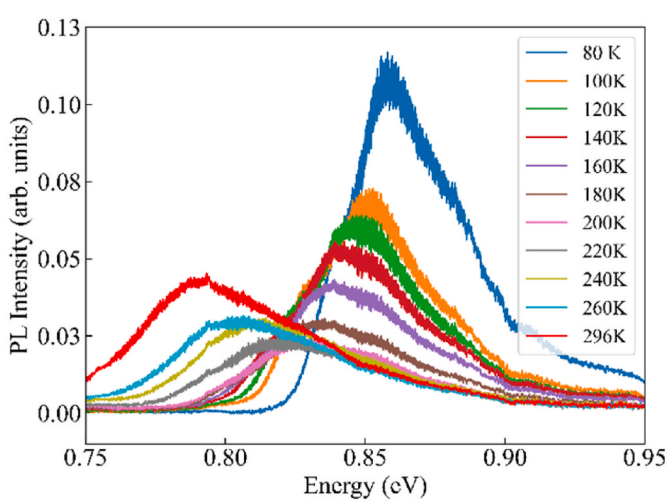

Fig. 11. Temperature dependence of PL spectra of a 10 µm patch with thickness 700 nm.

deviation. The linear fit gave a bulk component $J_{bulk} = 35$ mA/cm^2 and a surface component of 72 µA/cm. By assuming that the depletion region at -1V extends throughout the entire Ge epilayer, we estimated the minority carrier lifetime τ and the surface recombination velocity S_0 as:

$$\tau = \frac{qn_iW}{J_{bulk}} = 6.3ns, \tag{3}$$

and

$$S_0 = \frac{qn_iW}{J_{surf}} = 3 \times 10^6 \frac{cm}{s} \tag{4}$$

where q is the elementary charge, n_i is the intrinsic carrier concentration of Ge and W is the width of depletion region. The obtained values were close to those reported for Ge-on-Si photodiodes in literature [41]. It is important to note that no surface passivation was applied, which could lead to a substantial reduction of the surface recombination velocity.

The photoresponse was measured from 1100 nm to 1650 nm only for photodiodes with width of 480 µm, at modulation of 330 Hz, in top-illumination geometry. The responsivities at reverse bias voltage of 0V, 0.03V and 1V are reported in Fig. 12 (c). The misfit dislocation network formed at the Ge/Si interface, from an electrical perspective, is equivalent to a charged layer, which could effectively reduce the built-in electric field, thus reducing the responsivity at 0V. As shown by PL spectroscopy, the tensile strain allows to extend the band edge toward longer wavelength, and the responsivity maintained rather high values beyond $\lambda = 1550$ nm, reaching a value of ~20 mA/W at 1600 nm at a reverse bias voltage of 0.03 V. We notice from Fig. 12 (d) that the responsivity reached its maximum value at a very low reverse bias voltage of ~150 mV, opening the possibility to operate the device in a quasi-photovoltaic mode.

4. Conclusions

We successfully achieved selective epitaxial growth (SEG) of Ge on a SiO_2/Si patterned substrate. Our approach allows the fabrication of high-quality, well-controlled Ge microstructure with desirable optical properties. SEG allows patterning of Ge patches with high precision in size and position, and with high crystalline quality, which can enhance the integration of the photodiode with other components or structures. The strain characteristics, including the strain distribution and strain-induced splitting of vibrational modes and electronic states, influence the optical properties of the Ge material. The observed shifts and distributions provide valuable insights into the properties of Ge from polarization-dependent Raman shifts, with potential implications for the design of optoelectronic devices. By optimizing the patches size and strain, photodiodes whose spectral response can be adjusted to fulfill

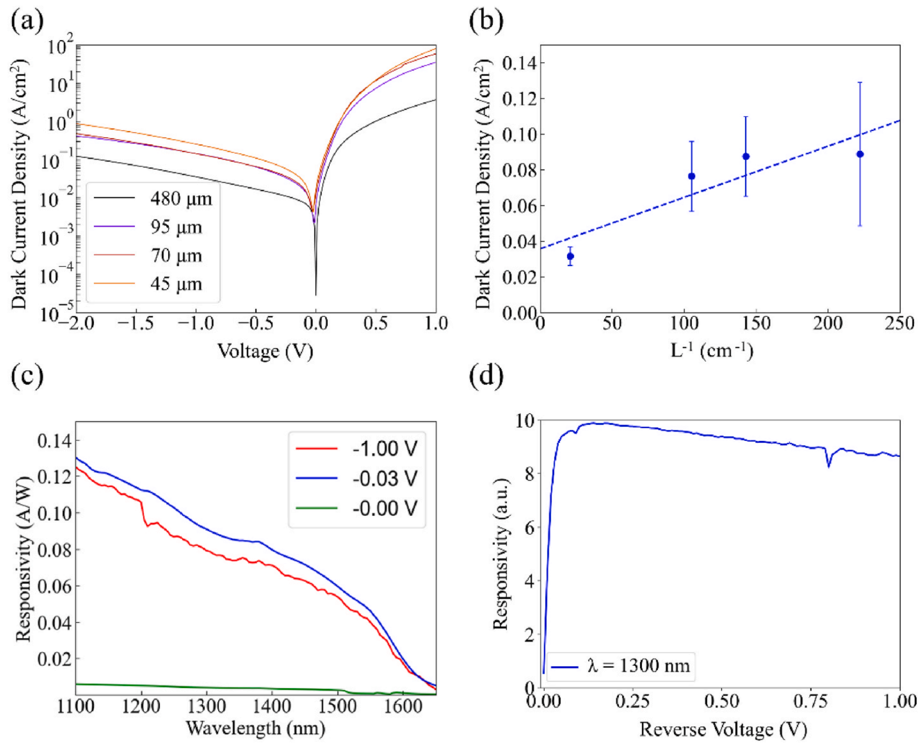

Fig. 12. (a) Dark current density as a function of the voltage for devices featuring lateral dimension of 480 μm (black line), 95 μm (purple line), 70 μm (red line) and 45 μm (orange line). (b) Dark current density as a function of the inverse of the lateral size of the photodiodes. (c) Responsivity at reverse bias voltages of 0V (green curve), 0.03 V (blue curve) and 1V (red curve) for one 480 μm photodiode. (d) Responsivity of the 480 μm device at λ = 1300 nm as a function of the reverse bias voltage.

specific requirements can be designed. A well-defined and intense PL peak at 0.8 eV indicates a high absorption efficiency at that energy, suggesting that the photodetector will be sensitive to light at wavelength longer than 1550 nm. Furthermore, we demonstrated that the high responsivity of relatively large photodiodes at longer wavelengths beyond 1550 nm, enhances their suitability for sensing applications and highlights the potential of strain engineering in optimizing photodiode properties, making it a valuable component for various applications in optoelectronics and photonics.

CRediT authorship contribution statement

Diana Ryzhak: Writing – original draft, Visualization, Investigation, Formal analysis, Data curation. **Agnieszka Anna Corley-Wiciak:** Writing – review & editing, Investigation. **Patrick Steglich:** Supervision, Methodology, Investigation, Conceptualization. **Yuji Yamamoto:** Writing – review & editing, Supervision, Methodology, Investigation. **Jacopo Frigerio:** Writing – original draft, Visualization, Validation, Supervision, Project administration, Investigation, Funding acquisition, Conceptualization. **Raffaele Giani:** Writing – review & editing, Investigation. **Andrea De Iacovo:** Writing – review & editing, Investigation, Funding acquisition, Conceptualization. **Davide Spirito:** Writing – original draft, Validation, Supervision, Investigation. **Giovanni Capellini:** Writing – original draft, Validation, Supervision, Project administration, Methodology, Funding acquisition, Conceptualization.

Declaration of competing interest

The authors declare that they have no known competing financial interests that could have appeared to influence the work reported in this paper. G.C. serves as co-guest editor to the present special issue.

Data availability

Data will be made available on request.

Acknowledgments

This work was partially funded by the ATTRACT Phase 2 Call for R&D&I Projects 2021 consortium under the VISIR2 grant. We acknowledge the process integration support form Daniel Steckler and Stefan Lischke.

Appendix A. Supplementary data

Supplementary data to this article can be found online at https://doi.org/10.1016/j.mssp.2024.108308.

References

[1] D. Marris-Morini, V. Vakarin, J.M. Ramirez, Q. Liu, A. Ballabio, J. Frigerio, M. Montesinos, C. Alonso-Ramos, X. Le Roux, S. Serna, D. Benedikovic, D. Chrastina, L. Vivien, G. Isella, Germanium-based integrated photonics from near- to mid-infrared applications, Nanophotonics 7 (2018) 1781–1793, https://doi.org/10.1515/nanoph-2018-0113.
[2] S. Lischke, A. Peczek, J.S. Morgan, K. Sun, D. Steckler, Y. Yamamoto, F. Korndörfer, C. Mai, S. Marschmeyer, M. Fraschke, A. Krüger, A. Beling, L. Zimmermann, Ultra-fast germanium photodiode with 3-dB bandwidth of 265 GHz, Nat. Photonics 15 (2021) 925–931, https://doi.org/10.1038/s41566-021-00893-w.
[3] G. Masini, S. Sahni, G. Capellini, J. Witzens, C. Gunn, High-Speed near infrared optical receivers based on Ge waveguide photodetectors integrated in a CMOS process, Adv. Opt. Technol. 2008 (2008) 1–5, https://doi.org/10.1155/2008/196572.
[4] E. Talamas Simola, V. Kiyek, A. Ballabio, V. Schlykow, J. Frigerio, C. Zucchetti, A. De Iacovo, L. Colace, Y. Yamamoto, G. Capellini, D. Grützmacher, D. Buca, G. Isella, CMOS-compatible bias-tunable dual-band detector based on GeSn/Ge/Si coupled photodiodes, ACS Photonics 8 (2021) 2166–2173, https://doi.org/10.1021/acsphotonics.1c00617.

[5] E.T. Simola, A. De Iacovo, J. Frigerio, A. Ballabio, A. Fabbri, G. Isella, L. Colace, Voltage-tunable dual-band Ge/Si photodetector operating in VIS and NIR spectral range, Opt Express 27 (2019) 8529, https://doi.org/10.1364/OE.27.008529.

[6] F. Cao, L. Liu, L. Li, Short-wave infrared photodetector, Mater, Today Off. 62 (2023) 327–349, https://doi.org/10.1016/j.mattod.2022.11.003.

[7] A.K. Sood, J.W. Zeller, R.A. Richwine, Y.R. Puri, H. Efstathiadis, P. Haldar, N. K. Dhar, D.L. Polla, SiGe based visible-NIR photodetector technology for optoelectronic applications, in: Moh Yasin, H. Arof, S.W. Harun (Eds.), Adv. Opt. Fiber Technol. Fundam. Opt. Phenom. Appl., InTech, 2015, https://doi.org/10.5772/59065.

[8] S.A. Claussen, K.C. Balram, E.T. Fei, T.I. Kamins, J.S. Harris, D.A.B. Miller, Selective area growth of germanium and germanium/silicon-germanium quantum wells in silicon waveguides for on-chip optical interconnect applications, Opt. Mater. Express 2 (2012) 1336, https://doi.org/10.1364/OME.2.001336.

[9] A. Mai, P. Steglich, C. Mai, S. Simon, R. Scholz, Electronic-photonic wafer-level technologies for fast prototyping and application specific solutions, in: 2019 PhotonIcs Electromagn. Res. Symp. - Spring PIERS-Spring, IEEE, Rome, Italy, 2019, pp. 249–255, https://doi.org/10.1109/PIERS-Spring46901.2019.9017528.

[10] Y. Yamamoto, G. Kozlowski, P. Zaumseil, B. Tillack, Low threading dislocation Ge on Si by combining deposition and etching, Thin Solid Films 520 (2012) 3216–3221, https://doi.org/10.1016/j.tsf.2011.10.095.

[11] A. Rastelli, H. Von Känel, Surface evolution of faceted islands, Surf. Sci. 515 (2002) L493–L498, https://doi.org/10.1016/S0039-6028(02)01998-2.

[12] J.T. Robinson, A. Rastelli, O. Schmidt, O.D. Dubon, Global faceting behavior of strained Ge islands on Si, Nanotechnology 20 (2009) 085708, https://doi.org/10.1088/0957-4484/20/8/085708.

[13] Z. Gai, W.S. Yang, R.G. Zhao, T. Sakurai, Macroscopic and nanoscale faceting of germanium surfaces, Phys. Rev. B 59 (1999) 15230–15239, https://doi.org/10.1103/PhysRevB.59.15230.

[14] B.W. Batterman, Hillocks, pits, and etch rate in germanium crystals, J. Appl. Phys. 28 (1957) 1236–1241, https://doi.org/10.1063/1.1722624.

[15] M. Brehm, H. Lichtenberger, T. Fromherz, G. Springholz, Ultra-steep side facets in multi-faceted SiGe/Si(001) Stranski-Krastanow islands, Nanoscale Res. Lett. 6 (2011) 70, https://doi.org/10.1186/1556-276X-6-70.

[16] M. Albani, R. Bergamaschini, A. Barzaghi, M. Salvalaglio, J. Valente, D.J. Paul, A. Voigt, G. Isella, F. Montalenti, Faceting of Si and Ge crystals grown on deeply patterned Si substrates in the kinetic regime: phase-field modelling and experiments, Sci. Rep. 11 (2021) 18825, https://doi.org/10.1038/s41598-021-98285-1.

[17] G. Capellini, M.D. Seta, F. Evangelisti, GeÕSi,100… islands: growth dynamics versus growth rate, J. Appl. Phys. 93 (2003).

[18] Y. Yamamoto, P. Zaumseil, T. Arguirov, M. Kittler, B. Tillack, Low threading dislocation density Ge deposited on Si (100) using RPCVD, Solid State Electron. 60 (2011) 2–6, https://doi.org/10.1016/j.sse.2011.01.032.

[19] O. Skibitzki, M.H. Zoellner, F. Rovaris, M.A. Schubert, Y. Yamamoto, L. Persichetti, L. Di Gaspare, M. De Seta, R. Gatti, F. Montalenti, G. Capellini, Reduction of threading dislocation density beyond the saturation limit by optimized reverse grading, Phys. Rev. Mater. 4 (2020) 103403, https://doi.org/10.1103/PhysRevMaterials.4.103403.

[20] Y. Yamamoto, P. Zaumseil, M.A. Schubert, B. Tillack, Influence of annealing conditions on threading dislocation density in Ge deposited on Si by reduced pressure chemical vapor deposition, Semicond. Sci. Technol. 33 (2018) 124007, https://doi.org/10.1088/1361-6641/aae574.

[21] H.-C. Luan, D.R. Lim, K.K. Lee, K.M. Chen, J.G. Sandland, K. Wada, L.C. Kimerling, High-quality Ge epilayers on Si with low threading-dislocation densities, Appl. Phys. Lett. 75 (1999) 2909–2911, https://doi.org/10.1063/1.125187.

[22] G. Wang, R. Loo, E. Simoen, L. Souriau, M. Caymax, M.M. Heyns, B. Blanpain, A model of threading dislocation density in strain-relaxed Ge and GaAs epitaxial films on Si (100), Appl. Phys. Lett. 94 (2009) 102115, https://doi.org/10.1063/1.3097245.

[23] C.L. Manganelli, M. Virgilio, O. Skibitzki, M. Salvalaglio, D. Spirito, P. Zaumseil, Y. Yamamoto, M. Montanari, W.M. Klesse, G. Capellini, Temperature dependence of strain–phonon coefficient in epitaxial Ge/Si(001): a comprehensive analysis, J. Raman Spectrosc. 51 (2020) 989–996, https://doi.org/10.1002/jrs.5860.

[24] A. Tarun, N. Hayazawa, H. Ishitobi, S. Kawata, M. Reiche, O. Moutanabbir, Mapping the "forbidden" transverse-optical phonon in single strained silicon (100) nanowire, Nano Lett. 11 (2011) 4780–4788, https://doi.org/10.1021/nl202599q.

[25] V. Prabhakara, T. Nuytten, H. Bender, W. Vandervorst, S. Bals, J. Verbeeck, Linearized radially polarized light for improved precision in strain measurements using micro-Raman spectroscopy, Opt Express 29 (2021) 34531, https://doi.org/10.1364/OE.434726.

[26] R. Ossikovski, Q. Nguyen, G. Picardi, J. Schreiber, Determining the stress tensor in strained semiconductor structures by using polarized micro-Raman spectroscopy in oblique backscattering configuration, J. Appl. Phys. 103 (2008) 093525, https://doi.org/10.1063/1.2917314.

[27] J.-H. Fournier-Lupien, S. Mukherjee, S. Wirths, E. Pippel, N. Hayazawa, G. Mussler, J.M. Hartmann, P. Desjardins, D. Buca, O. Moutanabbir, Strain and composition effects on Raman vibrational modes of silicon-germanium-tin ternary alloys, Appl. Phys. Lett. 103 (2013) 263103, https://doi.org/10.1063/1.4855436.

[28] A. Ogura, D. Kosemura, (Invited) anisotropoic strain evaluation in the finite Si area by surface plasmon enhanced Raman spectroscopy, ECS Trans. 64 (2014) 67–77, https://doi.org/10.1149/06406.0067ecst.

[29] M. Sistani, M.G. Bartmann, N.A. Güsken, R.F. Oulton, H. Keshmiri, M.A. Luong, E. Robin, M.I. Den Hertog, A. Lugstein, Stimulated Raman scattering in Ge nanowires, J. Phys. Chem. C 124 (2020) 13872–13877, https://doi.org/10.1021/acs.jpcc.0c02602.

[30] J.S. Reparaz, A. Bernardi, A.R. Goñi, M.I. Alonso, M. Garriga, Composition dependence of the phonon strain shift coefficients of SiGe alloys revisited, Appl. Phys. Lett. 92 (2008) 081909, https://doi.org/10.1063/1.2884526.

[31] C.L. Manganelli, M. Virgilio, M. Montanari, I. Zaitsev, N. Andriolli, S. Faralli, S. Tirelli, F. Dagnano, W.M. Klesse, D. Spirito, Tensile strained germanium microstructures: a comprehensive analysis of thermo-opto-mechanical properties, Phys. Status Solidi A 218 (2021) 2100293, https://doi.org/10.1002/pssa.202100293.

[32] G. Capellini, G. Kozlowski, Y. Yamamoto, M. Lisker, C. Wenger, G. Niu, P. Zaumseil, B. Tillack, A. Ghrib, M. de Kersauson, M. El Kurdi, P. Boucaud, T. Schroeder, Strain analysis in SiN/Ge microstructures obtained via Si-complementary metal oxide semiconductor compatible approach, J. Appl. Phys. 113 (2013) 013513, https://doi.org/10.1063/1.4772781.

[33] S.C. Jain, H.E. Maes, K. Pinardi, I. De Wolf, Stresses and strains in lattice-mismatched stripes, quantum wires, quantum dots, and substrates in Si technology, J. Appl. Phys. 79 (1996) 8145–8165, https://doi.org/10.1063/1.362678.

[34] S. Sonoi, R. Katamawari, M. Shimokawa, K. Inaba, J.A. Piedra-Lorenzana, T. Hizawa, J. Fujikata, Y. Ishikawa, Direct bandgap control by narrowing the germanium strip structure on silicon for C+L band photonic devices, IEEE J. Quant. Electron. 58 (2022) 1–9, https://doi.org/10.1109/JQE.2022.3203128.

[35] W. Van Roosbroeck, Theory of the flow of electrons and holes in germanium and other semiconductors, Bell Syst. Tech. J. 29 (1950) 560–607, https://doi.org/10.1002/j.1538-7305.1950.tb03653.x.

[36] S. Ishida, S. Kako, K. Oda, T. Ido, S. Iwamoto, Y. Arakawa, Suspended germanium cross-shaped microstructures for enhancing biaxial tensile strain, Jpn. J. Appl. Phys. 55 (2016) 04EH14, https://doi.org/10.7567/JJAP.55.04EH14.

[37] M. Virgilio, C.L. Manganelli, G. Grosso, G. Pizzi, G. Capellini, Radiative recombination and optical gain spectra in biaxially strained n -type germanium, Phys. Rev. B 87 (2013) 235313, https://doi.org/10.1103/PhysRevB.87.235313.

[38] M. Virgilio, T. Schroeder, Y. Yamamoto, G. Capellini, Radiative and non-radiative recombinations in tensile strained Ge microstrips: photoluminescence experiments and modeling, J. Appl. Phys. 118 (2015) 233110, https://doi.org/10.1063/1.4938026.

[39] H. Chen, P. Verheyen, P. De Heyn, G. Lepage, J. De Coster, S. Balakrishnan, P. Absil, G. Roelkens, J. Van Campenhout, Dark current analysis in high-speed germanium p-i-n waveguide photodetectors, J. Appl. Phys. 119 (2016) 213105, https://doi.org/10.1063/1.4953147.

[40] Y. Lin, K.H. Lee, B. Son, C.S. Tan, Low-power and high-detectivity Ge photodiodes by in-situ heavy as doping during Ge-on-Si seed layer growth, Opt Express 29 (2021) 2940, https://doi.org/10.1364/OE.405364.

[41] B. Arunachalam, Q. Rafhay, D. Roy, A. Kaminski-Cachopo, Simulation study of high-speed Ge photodetector dark and light current degradation, IEEE Trans. Device Mater. Reliab. 22 (2022) 410–416, https://doi.org/10.1109/TDMR.2022.3185671.